



# The high activity and stability of $\text{La}_{0.5}\text{Ba}_{0.5}\text{MnO}_3$ nanocubes in the oxidation of CO and $\text{CH}_4$

Shuhui Liang, Tongguang Xu, Fei Teng, Ruilong Zong, Yongfa Zhu \*

Department of Chemistry, Tsinghua University, Beijing 100084, PR China

## ARTICLE INFO

### Article history:

Received 17 June 2009

Received in revised form 19 December 2009

Accepted 22 January 2010

Available online 25 February 2010

### Keywords:

$\text{La}_{0.5}\text{Ba}_{0.5}\text{MnO}_3$

Nanocubes

Single crystal structure

Jahn–Teller distortion

CO oxidation

$\text{CH}_4$  oxidation

## ABSTRACT

$\text{La}_{0.5}\text{Ba}_{0.5}\text{MnO}_3$  nanocubes and nanoparticles were synthesized by hydrothermal and co-precipitation methods, respectively. The catalytic performances and thermal stabilities of the samples in the oxidation of CO and  $\text{CH}_4$  were evaluated.  $\text{La}_{0.5}\text{Ba}_{0.5}\text{MnO}_3$  nanocubes showed much higher catalytic activity and thermal stability in CO and  $\text{CH}_4$  oxidation compared with the nanoparticles. After running at 560 °C for 50 h under the reaction conditions in  $\text{CH}_4$  oxidation, the surface area of the nanoparticles decreased significantly, while the nanocubes well maintained their surface area. Jahn–Teller effect had a significant influence on the catalytic performances of  $\text{La}_{0.5}\text{Ba}_{0.5}\text{MnO}_3$  nanocubes and nanoparticles. The much higher catalytic activity and thermal stability of  $\text{La}_{0.5}\text{Ba}_{0.5}\text{MnO}_3$  nanocubes were mainly predominated by the perfect single crystal structure.

© 2010 Elsevier B.V. All rights reserved.

## 1. Introduction

$\text{La}_{1-x}\text{Ba}_x\text{MnO}_3$  manganites with perovskite structure have been widely used as oxidation catalysts, cathode materials in solid-oxide fuel cells and magnetic sensors [1–4]. They were mainly prepared using high temperature ceramic, co-precipitation, citrate routes, sol–gel, etc., which all need high temperature [5–8]. Recently,  $\text{La}_{0.5}\text{M}_{0.5}\text{MnO}_3$  ( $M = \text{Ca}, \text{Sr}, \text{Ba}$ ) cubes with single crystals have been obtained under hydrothermal conditions and their magnetization properties have been determined [9–14]. Urban et al. synthesized  $\text{La}_{1-x}\text{Ba}_x\text{MnO}_3$  ( $x = 0.3, 0.5, 0.6$ ) nanocubes and investigated the magnetic properties of the samples [14]. It is generally accepted that the single crystals exhibit different properties compared with the polycrystals. However, a little work has been done to elucidate the relationship between Jahn–Teller distortion and catalytic properties. Our group has reported the distinct catalytic property of the single crystal  $\text{La}_{0.5}\text{Sr}_{0.5}\text{MnO}_3$  cubes with a particle size of 1.5  $\mu\text{m}$ , and the catalytic activity is related to Jahn–Teller distortion [15,16]. Though the single crystal  $\text{La}_{0.5}\text{Ba}_{0.5}\text{MnO}_3$  nanocube is a potential catalytic oxidation material, few researchers have devoted to the study of its catalytic property up to now. Compared with the single crystal  $\text{La}_{0.5}\text{Sr}_{0.5}\text{MnO}_3$  cubes about 1.5  $\mu\text{m}$ ,  $\text{La}_{0.5}\text{Ba}_{0.5}\text{MnO}_3$  nanocubes with single crystal structure would show distinct catalytic

property. It is helpful for further research of the interaction between Jahn–Teller distortion and the catalytic properties, investigating the catalytic properties of  $\text{La}_{0.5}\text{Ba}_{0.5}\text{MnO}_3$  nanocubes in CO and  $\text{CH}_4$  oxidation, and it is also meaningful from the viewpoint of the synthesis of functional materials.

Herein,  $\text{La}_{0.5}\text{Ba}_{0.5}\text{MnO}_3$  single crystal nanocubes and polycrystalline nanoparticles were synthesized by hydrothermal and co-precipitation methods, respectively. The nanocubes were characterized by transmission electron microscopy (TEM), scan electron microscopy (SEM), high-resolution transmission electron microscopy (HRTEM), X-ray diffraction (XRD),  $\text{H}_2$ -temperature-programmed reduction (TPR), CO-temperature-programmed desorption (TPD),  $\text{CO}_2$ -TPD,  $\text{O}_2$ -TPD and Raman analysis. The catalytic properties and thermal stabilities of the  $\text{La}_{0.5}\text{Ba}_{0.5}\text{MnO}_3$  catalysts in the oxidation of CO and  $\text{CH}_4$  were researched.

## 2. Experiment

### 2.1. Synthesis of $\text{La}_{0.5}\text{Ba}_{0.5}\text{MnO}_3$ nanocubes and nanoparticles

The synthesis of  $\text{La}_{0.5}\text{Ba}_{0.5}\text{MnO}_3$  single crystal nanocubes was carried out under hydrothermal conditions as described previously [9,14].  $\text{La}(\text{NO}_3)_3 \cdot 6\text{H}_2\text{O}$ ,  $\text{Ba}(\text{CH}_3\text{COO})_2$ ,  $\text{KMnO}_4$ , and  $\text{MnCl}_2 \cdot 4\text{H}_2\text{O}$  were used as the starting materials, and KOH was used as the mineralization. All of the chemicals were analytical grade and used without purification. The mixture composition was in the ratio of  $7\text{Mn}^{2+}:3\text{MnO}_4^{2-}:5\text{Ba}^{2+}:5\text{La}^{3+}:1250\text{KOH}:3256\text{H}_2\text{O}$ , based on the

\* Corresponding author. Tel.: +86 10 62783586; fax: +86 10 62787601.  
E-mail address: [zhuyf@tsinghua.edu.cn](mailto:zhuyf@tsinghua.edu.cn) (Y. Zhu).

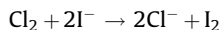
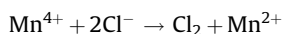
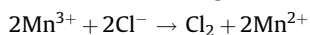
stoichiometric ratios of  $\text{La}_{0.5}\text{Ba}_{0.5}\text{MnO}_3$ . Typically, the starting chemicals were dissolved in about 15 mL of deionized water, and then 18.3 g of KOH was added to the solution under stirring. After 30 min of stirring, the mixture was poured into an autoclave (45 mL volume), and then subjected to hydrothermal treatment at 240 °C for 24 h. After cooling to room temperature naturally, the obtained products were filtered, washed several times with deionized water and ethanol until pH reaches 7–8, and dried in air at 80 °C for 24 h.

$\text{La}_{0.5}\text{Ba}_{0.5}\text{MnO}_3$  nanoparticles were prepared by co-precipitation method. The mixture solution of  $\text{La}(\text{NO}_3)_3 \cdot 6\text{H}_2\text{O}$ ,  $\text{Ba}(\text{CH}_3\text{COO})_2$ , and  $\text{MnCl}_2 \cdot 4\text{H}_2\text{O}$  at the stoichiometry above (1:1:2) was precipitated using KOH and  $\text{K}_2\text{CO}_3$  (1:1) mixed solution and made to pH = 11–12. After the mixture reacted for about 30 min, the obtained products were washed several times with deionized water until pH reaches 7–8. The depositions were evaporated and completely dried at 80 °C overnight in an oven. The obtained materials were crushed and calcined at 1200 °C for 8 h under flowing air, then the perovskite type oxide  $\text{La}_{0.5}\text{Ba}_{0.5}\text{MnO}_3$  nanoparticles were obtained.

## 2.2. Characterization

The morphologies and sizes of  $\text{La}_{0.5}\text{Ba}_{0.5}\text{MnO}_3$  samples were measured using TEM (JEOL1200EX) with 100 kV accelerating voltage of electron beam and SEM (KYKY 2800) with 15 keV acceleration voltage and 1.2 nA current. HRTEM (using a JEOL JEM-2010) was used to determine the surface structure of  $\text{La}_{0.5}\text{Ba}_{0.5}\text{MnO}_3$  nanocubes. The samples were characterized by XRD (Rigaku D/MAX-RB X-ray powder diffractometer), using Cu K $\alpha$  radiation ( $\lambda = 0.154$  nm), operating at 40 kV and 50 mA. Brunauer–Emmett–Teller (BET) surface areas of the catalysts were determined by  $\text{N}_2$  adsorption at –196 °C using a Tristar 2010 Chemical Adsorption Instrument. Raman spectra were measured at room temperature using a Jobin Yvon/Atago-Bussan T-64000 triple spectrometer with liquid nitrogen cooled CCD detector. The green line ( $\lambda = 514.5$  nm) of an Ar<sup>+</sup> laser was used to excite the Raman spectra, using a laser beam power of 10 mW on the sample. Inductively coupled plasma (ICP; Thermo Electron Corporation, IRIS Intrepid II XSP) was used for the determination of metal element concentration.

In order to determine the  $\text{Mn}^{3+}$  and  $\text{Mn}^{4+}$  state and oxygen content of the samples, iodometric titrations were performed, as previously described in the literature for related materials [17]. 30 mL of 0.5 N HCl and 25 mL of 0.16 M KI solution, excess in both cases, were added into a 500 mL flask. The flask was warmed to about 50 °C and around 0.22 g of  $\text{La}_{1-x}\text{Ba}_x\text{MnO}_{3\pm\delta}$  sample was added. The following reactions occurred:



After the sample dissolved completely, the flask was cooled in a dark place and its content was titrated with standard 0.02 N thiosulfate solution using starch as an indicator.

## 2.3. $\text{H}_2$ -TPR, CO-TPD, $\text{CO}_2$ -TPD and $\text{O}_2$ -TPD

$\text{H}_2$ -TPR (temperature-programmed reduction) experiment was performed on a conventional  $\text{H}_2$ -TPR instrument. 0.1 g of sample was placed in a quartz reactor and preheated in flowing 20%  $\text{O}_2$  in He at 500 °C for 30 min. After cooling to room temperature, it was reduced with a 5%  $\text{H}_2/\text{Ar}$  mixture (30 mL min<sup>–1</sup>) heating 10 °C min<sup>–1</sup> up to 800 °C.  $\text{H}_2$  was detected using mass spectrum.

CO-temperature-programmed desorption (TPD) measurement was performed on the same set-up used for TPR. 0.1 g of catalyst was heated at 500 °C for 30 min in He flow to remove pollutants adsorbed on the catalyst. Under the flowing He gas (40 mL min<sup>–1</sup>), the system was cooled naturally to room temperature. The sample was then saturated with CO at room temperature for 30 min. Excess of adsorbate was removed by allowing the sample to remain in He flow until no significant amount of adsorbate could be detected. The temperature ramped to 800 °C at a linear heating rate of 10 °C min<sup>–1</sup>. A mass spectrometer was used to monitor the *m/e* ratios 28 (CO) and 44 ( $\text{CO}_2$ ).

$\text{CO}_2$ -TPD measurement was carried out on the same instrument. 0.1 g of sample was treated in a He stream (40 mL min<sup>–1</sup>) for 0.5 h at 500 °C. After it was cooled to room temperature, the sample was then saturated with  $\text{CO}_2$  at room temperature for 30 min. The temperature ramped to 800 °C at a linear heating rate of 10 °C min<sup>–1</sup>.  $\text{CO}_2$  was detected by mass spectrum.

$\text{O}_2$ -TPD measurement was carried out with a flow system using He (40 mL min<sup>–1</sup>) as a carrier gas. 0.1 g of sample was treated for 0.5 h at 500 °C. After it was cooled to room temperature, the sample was then saturated with  $\text{O}_2$  at room temperature for 30 min. Then the temperature was raised at a constant rate of 10 °C min<sup>–1</sup> up to 800 °C, and oxygen desorbed was detected by mass spectrometer.

## 2.4. Catalytic oxidation measurement

The reactions of CO and  $\text{CH}_4$  oxidation were carried out in flow systems under atmospheric pressure. Catalyst (0.1 g) was loaded in a quartz reactor (inner diameter about 5 mm), with quartz beads packed at both ends of the catalyst bed. Before each run, the catalyst was flushed with air (100 mL min<sup>–1</sup>) at 500 °C for 1 h in order to remove adsorbed species from the surface, and then cooled to room temperature. For CO oxidation, a mixture gas of 2 vol.% CO and 98 vol.% air was fed into the catalyst bed at a gas hourly space velocity (GHSV, volume of gas/h  $\times$  volume of catalyst) of 12,000 h<sup>–1</sup>. For  $\text{CH}_4$  oxidation, a gas mixture of 1 vol.%  $\text{CH}_4$  and 99 vol.% air was fed into the catalyst bed at a flow rate of 100 mL min<sup>–1</sup>. The compositions of outlet gases were analyzed by an on-line gas chromatography with a GDX-403 GC-column (1.5 m  $\times$  4 mm, 100 °C) and a hydrogen flame ionization detector (FID).

## 3. Results and discussion

### 3.1. Morphology and structure of $\text{La}_{0.5}\text{Ba}_{0.5}\text{MnO}_3$ nanocubes and nanoparticles

Fig. 1 shows TEM, SAED, and HRTEM images of  $\text{La}_{0.5}\text{Ba}_{0.5}\text{MnO}_3$  nanocubes and nanoparticles. Fig. 1a indicates that the grain sizes of  $\text{La}_{0.5}\text{Ba}_{0.5}\text{MnO}_3$  particles range in 80–150 nm. Fig. 1b shows that the sample consists of cube-shaped crystallite. The average diameter of the cube is mainly in the range of 200–500 nm. The spots in the SAED patterns (insert of Fig. 1b) confirm the single-crystal structure of the nanocubes. Fig. 1c shows that the surface of the nanocubes is clean and has no sheathed amorphous phase, and the clear lattice fringes confirm the high crystallinity and the single crystalline nature (insert of Fig. 1c shows Fourier transform diffraction patterns of the HRTEM). The interplanar spacing is calculated to be 0.39 nm, which is consistent with the {1 1 0} plane of a cubic  $\text{La}_{0.5}\text{Ba}_{0.5}\text{MnO}_3$  crystal, indicating the preferred growth along the [1 0 0] direction.

Fig. 2 shows XRD patterns of  $\text{La}_{0.5}\text{Ba}_{0.5}\text{MnO}_3$  catalysts. No shift of the diffraction peaks were observed for  $\text{La}_{0.5}\text{Ba}_{0.5}\text{MnO}_3$  nanocubes and nanoparticles, all diffraction peaks of the samples were indexed to pseudo-cubic perovskite structure. ICP elemental analysis

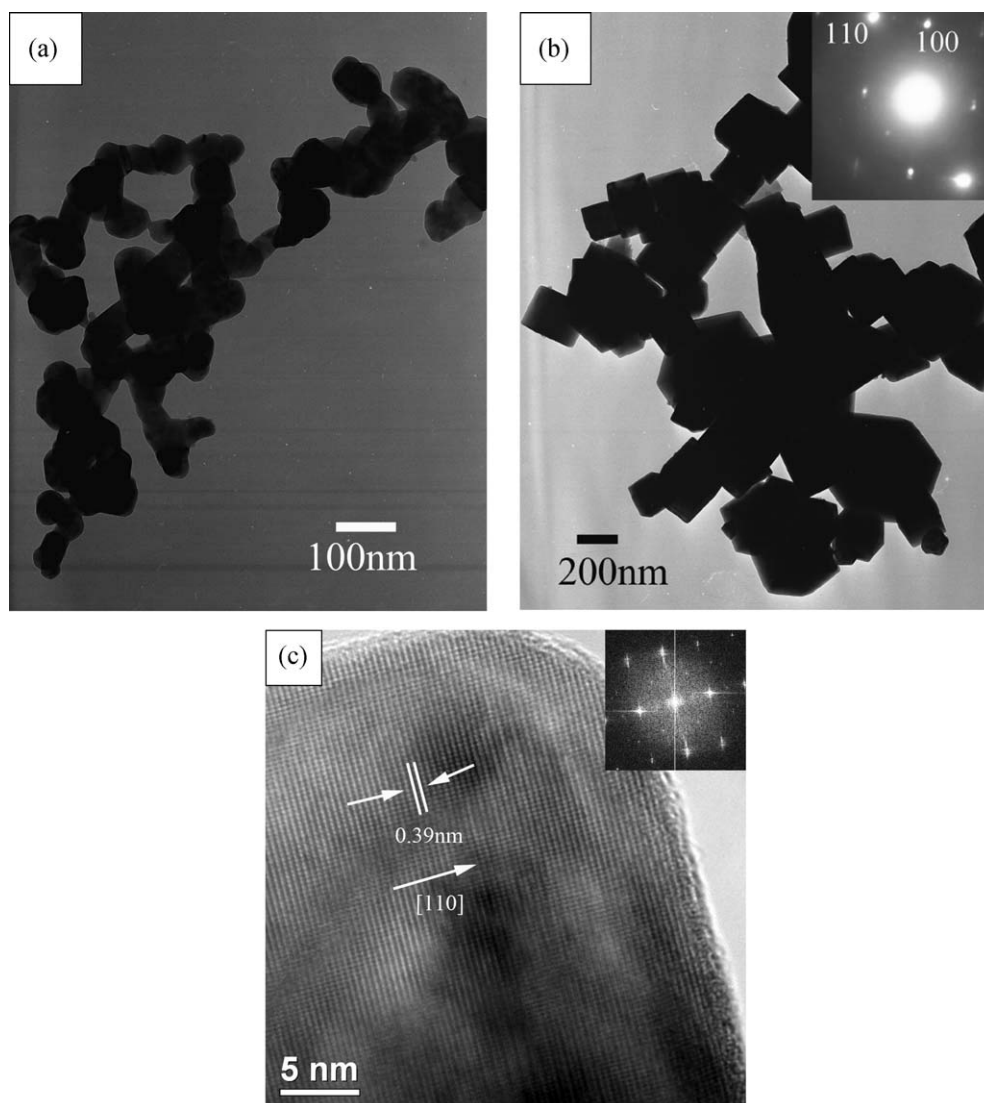


Fig. 1. TEM, HRTEM, and SAED images of  $\text{La}_{0.5}\text{Ba}_{0.5}\text{MnO}_3$  catalysts. (a) the nanoparticles; (b, c) the nanocubes.

indicated that the compositions of the samples were close to the stoichiometric ratios of  $\text{La}_{0.5}\text{Ba}_{0.5}\text{MnO}_3$  (La:Ba:Mn = 0.47:0.49:1 in the nanoparticles and La:Ba:Mn = 0.50:0.48:1 in the nanocubes). In addition, the BET surface areas of  $\text{La}_{0.5}\text{Ba}_{0.5}\text{MnO}_3$  nanoparticles and nanocubes were 15.8 and  $7.1 \text{ m}^2 \text{ g}^{-1}$ , respectively. The content of  $\text{Mn}^{3+}$  and  $\text{Mn}^{4+}$  can be calculated [9,17] from the titration results

( $\text{Mn}_{\text{ox}}$ ) knowing the total manganese content ( $\text{Mn}_{\text{t}}$ ) from the preparation data of the solids from the following equations:

$$\text{Mn}_{\text{t}} = n_1 \text{Mn}^{3+} + n_2 \text{Mn}^{4+}$$

$$\text{Mn}_{\text{ox}} = n_1 \text{Mn}^{3+} + 2n_2 \text{Mn}^{4+}$$

$$\text{Mn}^{3+} = 2\text{Mn}_{\text{t}} - \text{Mn}_{\text{ox}}$$

$$\text{Mn}^{4+} = \text{Mn}_{\text{ox}} - \text{Mn}_{\text{t}}$$

Oxygen content was evaluated from the cation composition based on the charge neutrality condition. Iodometric titrations results, the  $\text{Mn}^{3+}$  and  $\text{Mn}^{4+}$  state and oxygen content of the samples are given in Table 1. We observed that the percentage of  $\text{Mn}^{4+}$  in the nanocube (46% about 50%) was great larger than that in the nanoparticle (28%). Though the oxygen deficiency states were present both in the nanocubes and in the nanoparticles, the value of  $|\delta|$  for the nanocubes ( $|\delta| = 0.02$ ) was greatly smaller than that for the nanoparticles ( $|\delta| = 0.11$ ).

Figs. 3 and 4 show SEM/TEM images and XRD patterns of the products under different hydrothermal conditions, respectively. When the reaction temperature was lower than  $240^\circ\text{C}$ , or the reaction time was lower than 24 h, or the concentration of KOH

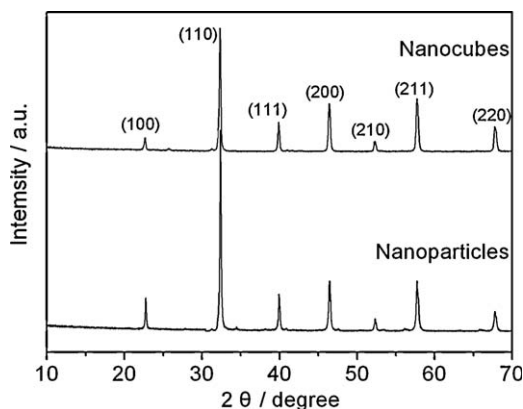


Fig. 2. XRD patterns of  $\text{La}_{0.5}\text{Ba}_{0.5}\text{MnO}_3$  nanocubes and nanoparticles.



**Table 1**

Iodometry results, calculated coefficients of manganese and oxygen in the formula  $\text{La}_{1-x}\text{Ba}_x\text{MnO}_{3\pm\delta}$  and the absolute values  $|\delta|$ .

Catalyst	$\text{Mn}_t$ (mol/100 g)	$\text{Mn}_{ox}$ (equivalent mol/100 g)	Coefficients for elements in formula			$ \delta $
			$\text{Mn}^{3+}$	$\text{Mn}^{4+}$	O	
Cubes	0.3978	0.5830	0.54	0.46	2.98	0.02
Nanoparticles	0.4207	0.5380	0.72	0.28	2.89	0.11

was lower than 20 M, the as-prepared products mainly consisted of both cubes and nanowires, and perovskite structure  $\text{La}_{0.5}\text{Ba}_{0.5}\text{MnO}_3$  was the main product, mixed with  $\text{La}(\text{OH})_3$ ,  $\text{BaMnO}_3$  and  $\text{K}_x\text{MnO}_2 \cdot n\text{H}_2\text{O}$ . Fig. 3a–c also shows that some nanowires and particles mix in the nanocubes. The pure complex  $\text{La}_{0.5}\text{Ba}_{0.5}\text{MnO}_3$  can only be obtained at 240 °C for 24 h in 20 M KOH. The reaction temperature, time, and the concentration of KOH all have significant influence on the formation of the  $\text{La}_{0.5}\text{Ba}_{0.5}\text{MnO}_3$  nanocubes. (The supporting information shows the effect of the reaction temperature, time, and mineralization

KOH on  $\text{La}_{0.5}\text{Ba}_{0.5}\text{MnO}_3$  nanocubes, and the forming mechanism of the nanocubes.) To further confirm the nanowires, they were measured by HRTEM, as shown in Fig. 3d. Fourier transition diffraction patterns of the HRTEM (insert of Fig. 3d) revealed the single crystalline nature of the nanowires, and can be indexed as the  $[010]$  zone axis of hexagonal  $\text{La}(\text{OH})_3$ . The HRTEM of the nanowires showed that the interplanar spacing was about 0.316 nm, which corresponded to the  $(010)$  plane of hexagonal  $\text{La}(\text{OH})_3$ . Wang and Li also reported that  $\text{La}(\text{OH})_3$  nanowires can be easily got in KOH by facile hydrothermal methods [18,19]. They

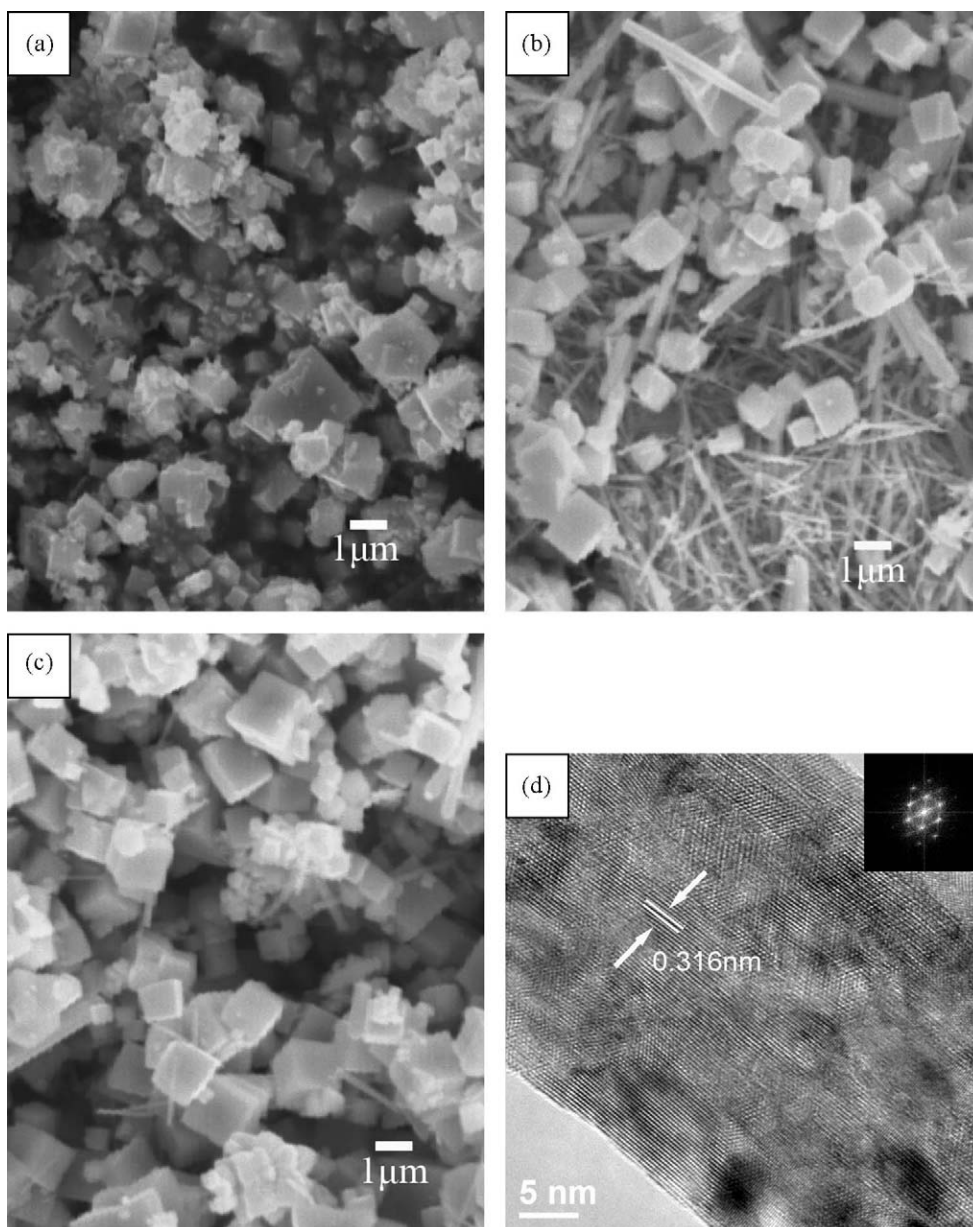


**Fig. 3.** SEM/TEM images of the products under different hydrothermal conditions. (a) 20 M KOH at 200 °C for 24 h; (b) 20 M KOH at 240 °C for 12 h; (c) 10 M KOH at 240 °C for 24 h; (d) the HRTEM of the nanorods mixed in the nanocubes.

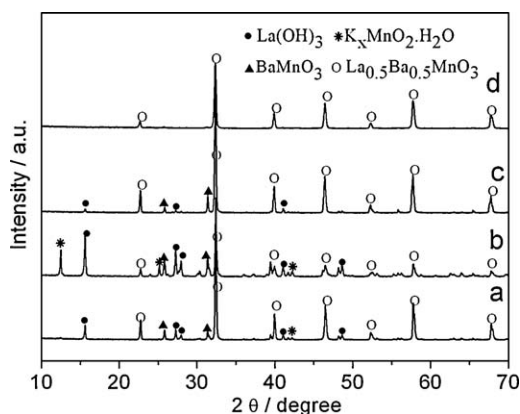


**Fig. 4.** XRD patterns of the products under different hydrothermal conditions. (a) 20 M KOH at 200 °C for 24 h; (b) 20 M KOH at 240 °C for 12 h; (c) 10 M KOH at 240 °C for 24 h; (d) 20 M KOH at 240 °C for 24 h.

also confirmed that the surface of  $\text{La}(\text{OH})_3$  nanowires consisted of hydroxyl groups, which may act as active sites for possible surface treatment and reaction.

### 3.2. Catalysis property

The activities of  $\text{La}_{0.5}\text{Ba}_{0.5}\text{MnO}_3$  nanocubes and nanoparticles in the oxidation of CO and  $\text{CH}_4$  were shown in Fig. 5a and b, respectively. The catalytic activity of the nanocubes in CO oxidation was much higher than that of the nanoparticles. For the nanoparticles,  $T_{10\text{ CO}}$  (the temperature of CO conversion 10%) was 124 °C, but  $T_{10\text{ CO}}$  was 105 °C for the nanocubes, which was lower 19 °C than the former.  $T_{50\text{ CO}}$  (the temperatures of CO conversion 50%) for the nanoparticles increased 32 °C compared to that of the nanocubes. The complete conversion temperatures for  $\text{La}_{0.5}\text{Ba}_{0.5}\text{MnO}_3$  nanoparticles and nanocubes were 200 and 160 °C, respectively. The former was higher 40 °C than the latter. Similarly, the catalytic activity of the nanocubes in  $\text{CH}_4$  oxidation was also much higher than that of the nanoparticles. Here the temperatures for 10%, 50% and 100% conversions of  $\text{CH}_4$  were designated as  $T_{10}$ ,  $T_{50}$  and  $T_{100}$ , respectively.  $T_{10}$ ,  $T_{50}$  and  $T_{100}$  for the nanoparticles increased 72, 88 and 100 °C compared to those for the nanocubes. The catalytic activities of the nanocubes in the oxidation of CO and  $\text{CH}_4$  were both obviously higher than those of the nanoparticles.

The combustion reactions of  $\text{CH}_4$  over  $\text{La}_{0.5}\text{Ba}_{0.5}\text{MnO}_3$  catalysts were performed at 560 °C for 50 h under the conditions of 1 vol.%  $\text{CH}_4$  and 99 vol.% air. The  $\text{CH}_4$  conversions at different durations of calcinations are shown in Fig. 5c. After running at 560 °C for 50 h, the conversion of  $\text{CH}_4$  over the  $\text{La}_{0.5}\text{Ba}_{0.5}\text{MnO}_3$  nanocubes was maintained at 97%; but that over the nanoparticles decreased from 58% to 47%.

In our previous work, Refs. [15,16] have reported the catalytic activity of  $\text{La}_{0.5}\text{Sr}_{0.5}\text{MnO}_3$  nanocubes. The different testing conditions, and the different crystal structures, morphologies of  $\text{La}_{0.5}\text{Sr}_{0.5}\text{MnO}_3$  and  $\text{La}_{0.5}\text{Ba}_{0.5}\text{MnO}_3$  may result for different data. In order to give a very clear explanation, we present a compared table among Refs. [15,16] and the manuscript in [supporting information \(Table S1\)](#). Furthermore, the different crystal structures, especially the Jahn–Teller distortion also can significantly influence the catalytic activities of the catalysts. At the same time, the grain sizes of the  $\text{La}_{0.5}\text{Ba}_{0.5}\text{MnO}_3$  nanocubes (200–500 nm) were greatly smaller than those of the  $\text{La}_{0.5}\text{Sr}_{0.5}\text{MnO}_3$  cubes (0.8–1.5  $\mu\text{m}$ ).

### 3.3. CO, $\text{CO}_2$ and $\text{O}_2$ adsorption and reducibility

CO-TPD was performed to explore CO adsorption on  $\text{La}_{0.5}\text{Ba}_{0.5}\text{MnO}_3$  catalysts, as shown in Fig. 6. A significant portion

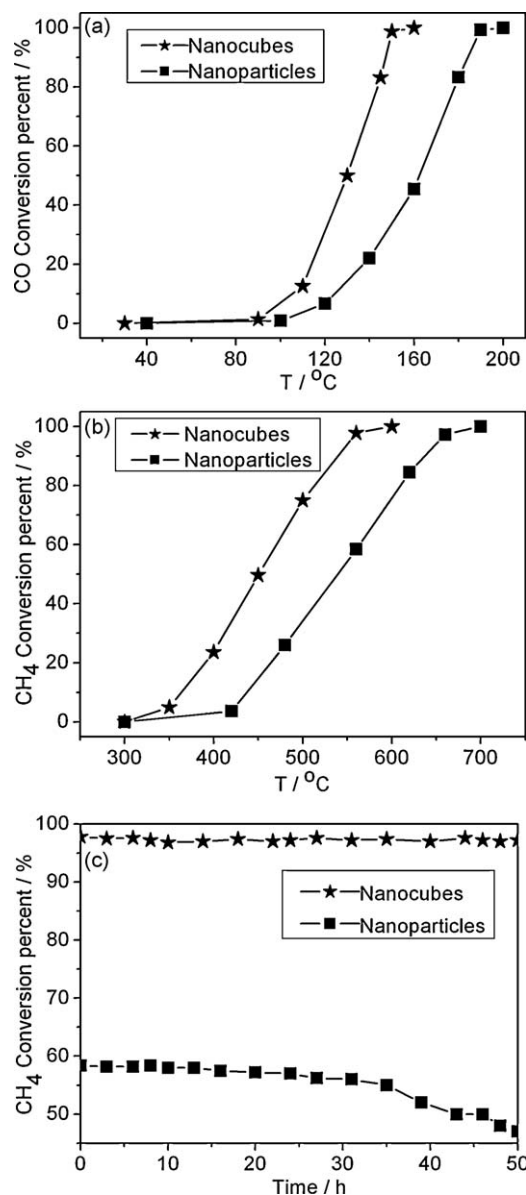


**Fig. 5.** (a, b) Conversion of CO and  $\text{CH}_4$  over  $\text{La}_{0.5}\text{Ba}_{0.5}\text{MnO}_3$  nanoparticles and nanocubes and (c) the variations of  $\text{CH}_4$  conversion over the catalysts with the duration at 560 °C.

of CO desorbed as a form of  $\text{CO}_2$  in the process, so the total adsorption amount of CO on the catalyst was consistent with the desorption amounts of both  $\text{CO}_2$  and CO. For  $\text{La}_{0.5}\text{Ba}_{0.5}\text{MnO}_3$  nanocubes, a CO desorption peak at about 645 °C was observed, whereas no obvious CO desorption peak was observed for  $\text{La}_{0.5}\text{Ba}_{0.5}\text{MnO}_3$  nanoparticles. Differences were also observed in  $\text{CO}_2$  desorption profiles in Fig. 6b. The  $\text{La}_{0.5}\text{Ba}_{0.5}\text{MnO}_3$  nanocubes showed two weak peaks at low temperatures of 187 and 250 °C, and one strong peak at a high temperature of 640 °C. However, only one wide  $\text{CO}_2$  desorption peak at a high temperature of 660 °C can be observed for  $\text{La}_{0.5}\text{Ba}_{0.5}\text{MnO}_3$  nanoparticles. The total adsorption amount of CO over the nanocubes (102.0  $\mu\text{mol g}^{-1}$ ) was larger than that over the nanoparticles (23.2  $\mu\text{mol g}^{-1}$ ), indicating that the nanocubes could provide more active sites than the nanoparticles.

The TPD profiles of  $\text{CO}_2$  absorbed on nanocubes and nanoparticles were studied to illustrate the different basic sites on these two catalysts, as shown in Fig. 7. Nanocubes showed two strong desorption peaks at 108 and 335 °C at lower temperature, and an

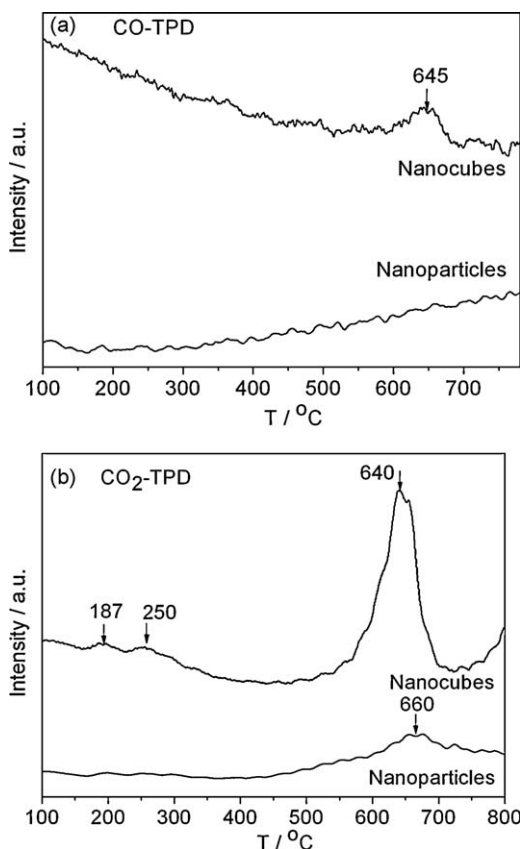


**Fig. 6.** TPD spectra after CO adsorption over  $\text{La}_{0.5}\text{Ba}_{0.5}\text{MnO}_3$  nanoparticles and nanocubes. (a) TPD of CO and (b) TPD of  $\text{CO}_2$  originated from the CO oxidation at the CO-TPD experiment.

obvious desorption course from 600 to 800 °C at higher temperature. Different from nanocubes, nanoparticles showed two weak desorption peaks at 70 and 430 °C at lower temperature, and a strong desorption peak at 580 °C at higher temperature. These desorption  $\text{CO}_2$  peaks can be attributed to the kinds of basic sites with different basicity. Based on the  $\text{CO}_2$ -TPD data, the adsorption amount of  $\text{CO}_2$  over the nanocubes ( $47 \mu\text{mol g}^{-1}$ ) was larger than that over the nanoparticles ( $7.4 \mu\text{mol g}^{-1}$ ) at lower temperature ( $T < 500$  °C), indicating that the nanocubes could provide more active sites than the nanoparticles. But at higher temperature ( $T > 500$  °C), the adsorption amount of  $\text{CO}_2$  over the nanoparticles ( $43.4 \mu\text{mol g}^{-1}$ ) was much larger than that over the nanocubes ( $3.2 \mu\text{mol g}^{-1}$ ). The basic strength of the catalyst meant the ability of getting H from  $\text{CH}_4$ , the higher number of strongly basic centers was consistent with the stronger of the basic center of the catalyst

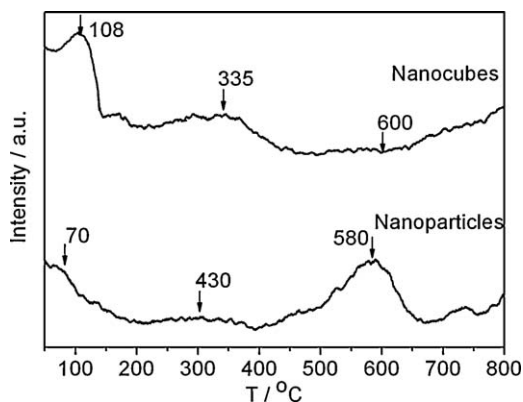


**Fig. 7.**  $\text{CO}_2$ -TPD profiles of  $\text{La}_{0.5}\text{Ba}_{0.5}\text{MnO}_3$  nanoparticles and nanocubes.

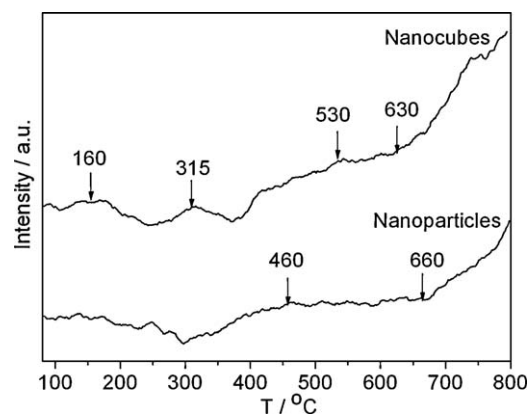


**Fig. 8.**  $\text{O}_2$ -TPD profiles of  $\text{La}_{0.5}\text{Ba}_{0.5}\text{MnO}_3$  nanoparticles and nanocubes.

surface and facilitating the generation of reactive oxygen species and activation of  $\text{CH}_4$ .

TPD spectra of  $\text{O}_2$  over both  $\text{La}_{0.5}\text{Ba}_{0.5}\text{MnO}_3$  catalysts are shown in Fig. 8. For  $\text{La}_{0.5}\text{Ba}_{0.5}\text{MnO}_3$  nanocubes, the desorption peaks of oxygen at 160, 315 and 530 °C resulted from the oxygen adsorbed on the catalyst surface. The strong oxygen desorption peak at higher temperature from 630 to 800 °C was referred to the reduction of  $\text{Mn}^{4+}$  ions to  $\text{Mn}^{3+}$  accompanied with the evolution of equivalent lattice oxygen. For the nanoparticles, the adsorbed oxygen desorption peak was broad at higher temperature 460 °C. The lattice oxygen desorption peak, resulted from the reduction of  $\text{Mn}^{4+}$  ions to  $\text{Mn}^{3+}$ , was strong extending from 660 up to 800 °C (where the experiment was stopped). The adsorbed oxygen amounts over the  $\text{La}_{0.5}\text{Ba}_{0.5}\text{MnO}_3$  nanocubes and nanoparticles were 14.2 and  $7.2 \mu\text{mol g}^{-1}$ , respectively. The lattice oxygen amounts over the nanocubes and nanoparticles were 23.6 and  $14.3 \mu\text{mol g}^{-1}$ , respectively. The temperatures of the adsorption and lattice oxygen desorption over the nanocubes both were lower than those over the nanoparticles, indicating that the nanocubes can more easily release active oxygen than the nanoparticles. This was consistent with the TPD data of  $\text{CO}_2$ .

$\text{H}_2$ -TPR profiles of the  $\text{La}_{0.5}\text{Ba}_{0.5}\text{MnO}_3$  samples were performed to investigate the relative reducibility, as shown in Fig. 9.  $\text{La}_{0.5}\text{Ba}_{0.5}\text{MnO}_3$  nanocubes showed a major peak at 390 °C associated with a weak peak at slightly high temperature 495 °C. The major peak at about 390 °C can be attributed to the reduction of  $\text{Mn}^{4+}$  to  $\text{Mn}^{3+}$  over  $\text{La}_{0.5}\text{Ba}_{0.5}\text{MnO}_3$  nanocubes. The shoulder at high temperature 495 °C maybe due to a single electron reduction of  $\text{Mn}^{3+}$  located in coordination-unsaturated microenvironments [15].  $\text{La}_{0.5}\text{Ba}_{0.5}\text{MnO}_3$  nanoparticles showed one broad reduction peak in the range of 290–540 °C. The major peak was about at 465 °C, which was attributed to the reduction of  $\text{Mn}^{4+}$  to  $\text{Mn}^{3+}$ . XRD diffraction patterns (Fig. 9b) after  $\text{H}_2$ -TPR also demonstrated that the perovskite structures of the nanocubes and nanoparticles were remained. The further reduction of  $\text{Mn}^{3+}$  to  $\text{Mn}^{2+}$  did not occur in the range of 800 °C. The perovskite structure ( $\text{La}_{0.5}\text{Ba}_{0.5}\text{MnO}_{3-\delta}$  intermediate) was very stable up to 800 °C, which was partly reduced from  $\text{Mn}^{4+}$  to  $\text{Mn}^{3+}$ . The reduction processes of  $\text{La}_{0.5}\text{Ba}_{0.5}\text{MnO}_3$  nanocubes and nanoparticles were very different from those of  $\text{La}_{0.5}\text{Sr}_{0.5}\text{MnO}_3$  cubes and nanoparticles, which were reduced from  $\text{Mn}^{3+}$  to  $\text{Mn}^{2+}$  about in the temperature region 600–800 °C under the similar condition [16]. The perovskite structure of  $\text{La}_{0.5}\text{Ba}_{0.5}\text{MnO}_3$  maybe seriously different from  $\text{La}_{0.5}\text{Sr}_{0.5}\text{MnO}_3$  [9]. The consumed amounts of  $\text{H}_2$  of the  $\text{La}_{0.5}\text{Ba}_{0.5}\text{MnO}_3$  nanocubes and nanoparticles were about 2.62 and  $1.64 \mu\text{mol g}^{-1}$ . The consumed amounts of  $\text{H}_2$  to some extent reflected the thermally desorbed quantity of oxygen over the samples. The desorbed quantity oxygen over  $\text{La}_{0.5}\text{Ba}_{0.5}\text{MnO}_3$



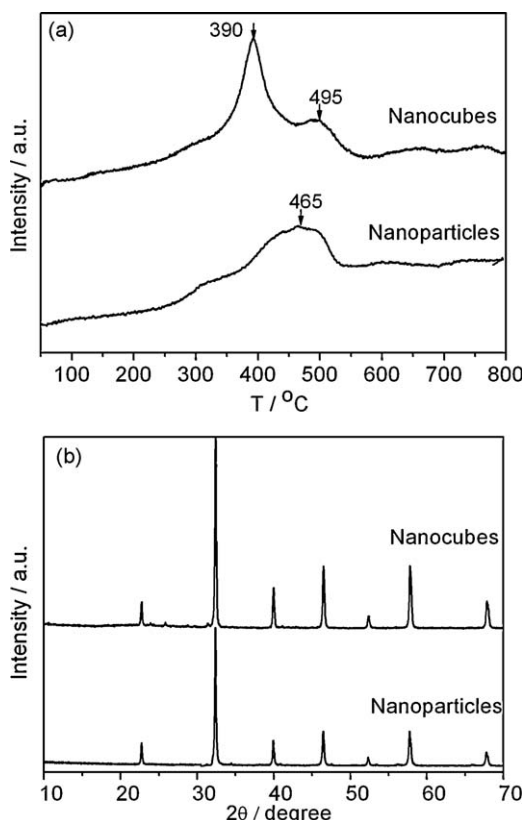


Fig. 9. (a) H<sub>2</sub>-TPR profiles of La<sub>0.5</sub>Ba<sub>0.5</sub>MnO<sub>3</sub> nanoparticles and nanocubes and (b) XRD patterns of La<sub>0.5</sub>Ba<sub>0.5</sub>MnO<sub>3</sub> nanoparticles and nanocubes after H<sub>2</sub>-TPR run.

nanocubes corresponding to the reduction of Mn<sup>4+</sup> to Mn<sup>3+</sup> and the removal of the non-stoichiometric excess oxygen accommodated within the lattice on the nanocubes was larger than that on the nanoparticles. The center positions of their reduction peaks for the nanocubes slightly shifted to lower temperatures than those of the nanoparticles, indicating the easy reducibility of the nanocubes. This was consistent with the result of O<sub>2</sub>-TPD.

#### 3.4. Effect of Jahn–Teller distortion on the high catalytic activity of La<sub>0.5</sub>Ba<sub>0.5</sub>MnO<sub>3</sub> nanocubes

Fig. 10 shows Raman spectra of La<sub>0.5</sub>Ba<sub>0.5</sub>MnO<sub>3</sub> nanocubes and nanoparticles. Only one main peak at about 650 cm<sup>−1</sup> was observed for La<sub>0.5</sub>Ba<sub>0.5</sub>MnO<sub>3</sub> nanocubes. La<sub>0.5</sub>Ba<sub>0.5</sub>MnO<sub>3</sub> nanoparticles showed three main peaks at about 400, 530 and 640 cm<sup>−1</sup>. The peaks at about 640 cm<sup>−1</sup> were related to the extension of Mn–

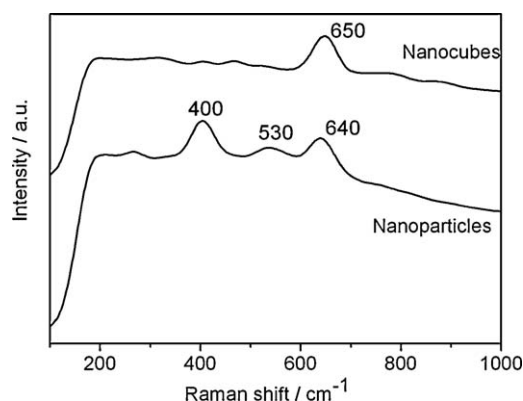


Fig. 10. Raman spectra of La<sub>0.5</sub>Ba<sub>0.5</sub>MnO<sub>3</sub> nanoparticles and nanocubes.

O in MnO<sub>6</sub> units [20]. The peak at 400 and 530 cm<sup>−1</sup> reflects the extension and compression of Mn–O bond pairs, which was directly correlated with Jahn–Teller distortion [21–24]. La<sub>0.5</sub>Ba<sub>0.5</sub>MnO<sub>3</sub> nanocubes did not show the bands at 400 and 530 cm<sup>−1</sup>, which resulted from the smaller Jahn–Teller distortion of the ideal cubic structure. The coordination oxygen atoms of Mn<sup>3+</sup>O<sub>6</sub> can form Jahn–Teller distorted octahedral, whereas Mn<sup>4+</sup> ions in Mn<sup>4+</sup>O<sub>6</sub> units have almost undistorted coordination. Iodometric titrations results also showed the great larger percent of Mn<sup>4+</sup> in the nanocubes, which well agreed with the Raman results. The dz<sup>2</sup> orbitals of Mn<sup>3+</sup>, associated with long Mn<sup>3+</sup>–O bonds in the Jahn–Teller distorted Mn<sup>3+</sup>O<sub>6</sub> octahedra, formed zigzag chains [25]. This ordering of Mn<sup>3+</sup>O<sub>6</sub> would entail displacements of Mn<sup>4+</sup>O<sub>6</sub> octahedra. Charge ordering was accompanied by orbital ordering, so the mobility of charge carriers (Mn<sup>3+</sup> → Mn<sup>4+</sup>) in the nanocubes with small Jahn–Teller distortion was facile. The small Jahn–Teller distortion of the nanocubes contributed to the ease reduction of the sample, which was agreed well with the H<sub>2</sub>-TPR results.

In general, BET surface area is a main factor that may influence the catalytic activity of catalyst. The BET surface area of La<sub>0.5</sub>Ba<sub>0.5</sub>MnO<sub>3</sub> nanoparticles is much larger than that of the nanocubes. However, the catalytic activities in the oxidation CO and CH<sub>4</sub> of the nanocubes are both higher than those of the nanoparticles. The results indicate that the catalytic activities are not significantly correlated with BET surface areas. The catalytic property maybe governed by the active sites in surface of the catalysts [26,27]. Based on CO-TPD data, La<sub>0.5</sub>Ba<sub>0.5</sub>MnO<sub>3</sub> nanocubes have much more activity sites than the nanoparticles. The higher catalytic activities of the nanocubes for CO and CH<sub>4</sub> oxidations can be attributed to the active sites and the easily released active oxygen, respectively.

CO chemisorption is directly related to the CO oxidation over La<sub>0.5</sub>Ba<sub>0.5</sub>MnO<sub>3</sub> samples [28]. The chemisorption of CO onto the catalysts involves the way in which CO attach to the coordination sites of Mn ions. Mn ions act as active centers for CO chemisorption. The 5σ electrons and empty 2π\* orbitals of CO can coordinate with d orbitals and d electrons of Mn ions, respectively [29]. Jahn–Teller distortion is an essence factor to govern CO chemisorption on La<sub>0.5</sub>Ba<sub>0.5</sub>MnO<sub>3</sub> nanoparticles and nanocubes. The small degree of Jahn–Teller distortion in La<sub>0.5</sub>Ba<sub>0.5</sub>MnO<sub>3</sub> nanocubes enhances the mobility of Mn<sup>3+</sup> → Mn<sup>4+</sup> charge transfer. Therefore, the average positive charge of Mn ions is higher and the average radius of Mn ions is smaller in the nanocubes than those in the nanoparticles. This makes the nanocubes capable of adsorbing more CO molecules. So the nanocubes can desorb more CO and have much more activity sites. Furthermore, the small degree of Jahn–Teller distortion in the nanocubes makes Mn<sup>3+</sup>–O–Mn<sup>4+</sup> have a bond angle of 180°, favoring electron transfer. Therefore, the nanocubes can be reduced at lower temperature compared with the nanoparticles. This result is consistent with H<sub>2</sub>-TPR results.

The mechanism of CO oxidation over La<sub>0.5</sub>Ba<sub>0.5</sub>MnO<sub>3</sub> samples is suggested that the adsorbed CO on Mn site reacts with the lattice oxygen, as we have reported that the mechanism over La<sub>0.5</sub>Sr<sub>0.5</sub>MnO<sub>3</sub> cubes. Three factors of the CO chemisorption, the supply of lattice oxygen and the transformation of adsorption oxygen into lattice oxygen have significant influences on the catalytic property of La<sub>0.5</sub>Ba<sub>0.5</sub>MnO<sub>3</sub> catalysts. The high catalytic activity of the nanocubes maybe resulted from the following three factors. First, the nanocubes can adsorb more CO molecules than the nanoparticles. Second, the nanocubes can be reduced at slightly lower temperature based on the H<sub>2</sub>-TPR results. Third, the mobility of Mn<sup>3+</sup> → Mn<sup>4+</sup> charge carriers is enhanced in the nanocubes. It is easy for the nanocubes to reinforce lattice oxygen by the charge transfer between MnO<sub>6</sub> octahedral.

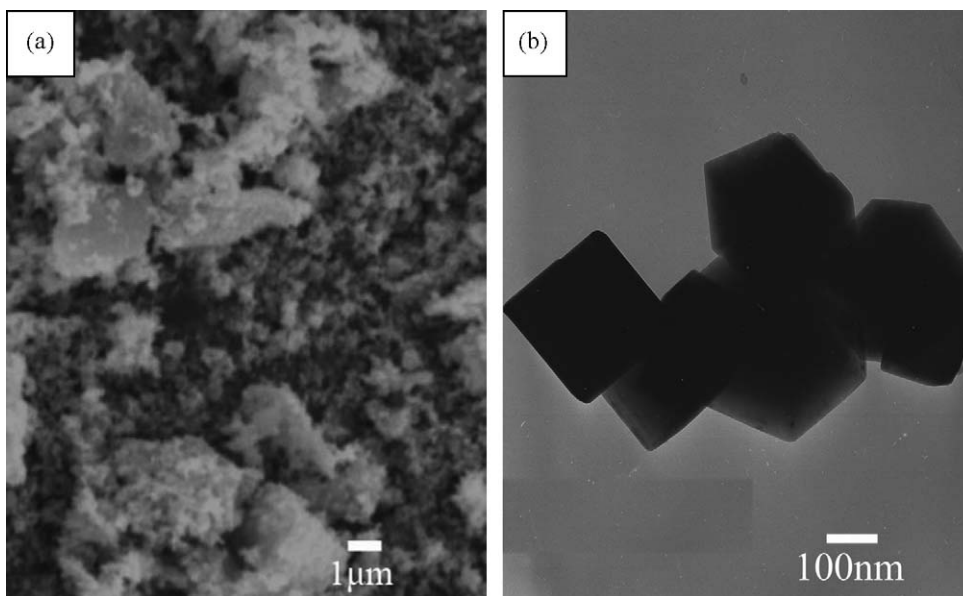


Fig. 11. TEM/SEM images of  $\text{La}_{0.5}\text{Ba}_{0.5}\text{MnO}_3$  nanoparticles and nanocubes after reaction at  $560^\circ\text{C}$  for 50 h.

Methane oxidation on metal oxides is known to follow a redox mechanism [30–33]. The oxidation of methane takes place by means of the lattice oxygen from the catalyst. The catalytic activities of  $\text{La}_{0.5}\text{Ba}_{0.5}\text{MnO}_3$  nanocubes are determined mainly by lattice oxygen. The stronger of the basic center of the catalyst surface is consistent with the better of generation reactive oxygen species. Therefore, the high catalytic activity of the nanocubes can be attributed to the ease supply of lattice oxygen, the enhancement of  $\text{Mn}^{3+} \rightarrow \text{Mn}^{4+}$  charge mobility, and the stronger of basic center of the catalyst surface at lower temperature.

### 3.5. Effect of single crystal and nanocube structure on the high stability

Compared with the nanoparticles, the nanocubes showed much higher stability at high temperature. A significant amount of water vapor was produced during this process, which would accelerate the sintering of the catalysts at high temperature. The TEM and SEM images of the nanoparticles and nanocubes after reaction for 50 h at  $560^\circ\text{C}$  (thermal stability test) were showed in Fig. 11. After thermal stability test, an obvious reunion took place for the nanoparticles catalyst, even about  $5\ \mu\text{m}$  great grains occurred. But for the nanocubes, agglomeration or grow up did not happen, they all kept the perfect nanocubes shape. After the reaction was complete, the surface area of the nanocubes decreased slightly to  $6.5\ \text{m}^2\ \text{g}^{-1}$  (the surface area of the nanocubes was  $7.1\ \text{m}^2\ \text{g}^{-1}$  before stability reaction), whereas that of the nanoparticles decreased significantly from  $15.8$  to  $3.2\ \text{m}^2\ \text{g}^{-1}$ .

It is obvious that the single crystal nanocube has higher thermal stability than the nanoparticles. Several pertinent factors should be considered. First, the surface-to-volume ratio of the nanocubes is larger than that of the nanoparticles, and thus there is a smaller driving force to sinter. Second, the contact area among the nanocubes maybe small, which may also hinder sintering of the nanocubes. Finally, the perfect single crystal structure may also contribute to the stability. The nanocube shape and the perfect single crystal structure mainly contribute to the high stability of the nanocube catalyst. The perfect single crystal structure and the little defect structure decide the high stability of the nanocubes.

The nanocubes  $\text{La}_{0.5}\text{Ba}_{0.5}\text{MnO}_3$  not only showed high catalytic activity but also had high thermal stability compared to the nanoparticles. Considering our previous work,  $\text{La}_{0.5}\text{Sr}_{0.5}\text{MnO}_3$  cube

(about  $0.8\text{--}1.5\ \mu\text{m}$ ) catalyst showed a lower activity than the nanoparticle catalyst in CO and  $\text{CH}_4$  oxidation, while the catalytic activity of the  $\text{La}_{0.5}\text{Sr}_{0.5}\text{MnO}_3$  cubes significantly increased at higher temperature compared to the corresponding nanoparticles. Furthermore, the catalytic activity of  $\text{La}_{0.5}\text{Ba}_{0.5}\text{MnO}_3$  nanocubes in CO oxidation was even higher than  $\text{MnO}_2$  nanorods [34].

It gives us a revelation, design and synthesis nanocubes with much smaller size is a very effective means to get high catalytic activity and high thermal stability catalysts.

## 4. Conclusions

$\text{La}_{0.5}\text{Ba}_{0.5}\text{MnO}_3$  nanocubes with pseudo-cubic structures were synthesized.  $\text{La}_{0.5}\text{Ba}_{0.5}\text{MnO}_3$  nanocubes showed a higher activity for CO and  $\text{CH}_4$  oxidation than the nanoparticles. CO chemisorption, the supply of lattice oxygen, and the mobility of  $\text{Mn}^{3+} \rightarrow \text{Mn}^{4+}$  charge carriers had significant influences on the catalytic property of the nanocubes for CO oxidation. The enhancement of  $\text{Mn}^{3+} \rightarrow \text{Mn}^{4+}$  charge mobility of the nanocubes was responsible for the high catalytic activity for  $\text{CH}_4$ . A high thermal stability of the  $\text{La}_{0.5}\text{Ba}_{0.5}\text{MnO}_3$  nanocubes against calcination was observed, and a high activity for  $\text{CH}_4$  oxidation was maintained. In conclusion, Jahn–Teller distortion and the perfect crystal geometry figure determined the high catalytic activities of  $\text{La}_{0.5}\text{Ba}_{0.5}\text{MnO}_3$  nanocubes in the oxidation of CO and  $\text{CH}_4$ .

## Acknowledgments

This work was partly supported by Chinese National Science Foundation (20433010 and 20571047) and National Basic Research Program of China (2007CB613303).

## Appendix A. Supplementary data

Supplementary data associated with this article can be found, in the online version, at doi:10.1016/j.apcatb.2010.01.025.

## References

- [1] Y. Tian, D.R. Chen, X.L. Jiao, Chem. Mater. 18 (2006) 6088.
- [2] S. Cimino, S. Colonna, S.D. Rossi, M. Faticanti, L. Lisi, I. Pettiti, P. Portaz, J. Catal. 205 (2002) 309.
- [3] C.N.R. Rao, J. Phys. Chem. B 104 (2000) 5877.



- [4] S. Jin, T.H. Tiefel, M.M. Cormack, R.A. Fastnacht, R. Ramesh, L.H. Chen, *Science* 264 (1994) 413.
- [5] S. Bilger, E. Syskakis, A. Naoumidia, H. Nickel, *J. Am. Ceram. Soc.* 75 (1992) 964.
- [6] R.J.H. Voorhoeve, J.P. Remeika, L.E. Trimble, *Ann. N. Y. Acad. Sci.* 272 (1976) 3.
- [7] M.S.G. Baythoun, F.R. Sale, *J. Mater. Sci.* 17 (1982) 2757.
- [8] T. Nakamura, M. Misono, T. Uchijima, Y. Yoneda, *Nippon Kagaku Kaishi* (1978) 1462.
- [9] J. Spooren, R.I. Walton, F. Millange, *J. Mater. Chem.* 15 (2005) 1542.
- [10] D. Zhu, H. Zhu, Y. Zhang, *Appl. Phys. Lett.* 80 (2002) 1634.
- [11] D. Zhu, H. Zhu, Y. Zhang, *J. Cryst. Growth* 249 (2003) 172.
- [12] J. Liu, H. Wang, M. Zhu, B. Wang, H. Yan, *Mater. Res. Bull.* 38 (2003) 817.
- [13] J. Spooren, A. Rumpelcker, F. Millange, R.I. Walton, *Chem. Mater.* 15 (2003) 1401.
- [14] J.J. Urban, L. Ouyang, M.H. Jo, D.S. Wang, H. Park, *Nanoletters* 4 (2004) 1547.
- [15] S.H. Liang, F. Teng, G. Bulgan, Y.F. Zhu, *J. Phys. Chem. C* 111 (2007) 16742.
- [16] F. Teng, W. Han, S.H. Liang, G. Bulgan, R.L. Zong, Y.F. Zhu, *J. Catal.* 250 (2007) 1.
- [17] A.A. Leontiou, A.K. Ladavos, G.S. Armatas, P.N. Trikalitis, P.J. Pomonis, *Appl. Catal. A: Gen.* 263 (2004) 227.
- [18] X. Wang, Y.D. Li, *Angew. Chem. Int. Ed.* 41 (2002) 4790.
- [19] X. Wang, Y.D. Li, *Chem. Eur. J.* 9 (2003) 5627.
- [20] J.A. Rodriguez, *J. Phys. Chem.* 179 (1994) 5758.
- [21] V.B. Podobedov, A. Webet, D.B. Romero, J.P. Rice, H.D. Drew, *Solid State Commun.* 105 (1998) 589.
- [22] A.E. Pantoja I, H.J. Trodahl, R.G. Buckley, Y. Tomioka, Y. Tokura, *J. Phys. Condens. Matter* 13 (2001) 3741.
- [23] K. Yamamoto, T. Kimura, T. Ishikawa, T. Katsufuji, Y. Tokura, *Phys. Rev. B* 61 (2000) 61.
- [24] M.N. Iliev, M.V. Abrashev, *J. Raman Spectrosc.* 32 (2001) 805.
- [25] V.B. Podobedov, A. Weber, *Phys. Rev. B* 58 (1998) 43.
- [26] R. Bindu, S.K. Pandey, A. Kumar, S. Khalid, A.V. Pimpale, *J. Phys.: Condens. Matter* 17 (2005) 6393.
- [27] Y. Chen, H.M. Yuan, G. Tian, G.H. Zhang, S.H. Feng, *J. Solid State Chem.* 180 (2007) 167.
- [28] B. Viswanathan, *Catal. Rev: Sci. Eng.* 34 (1992) 337.
- [29] J.W. Mullin, *Crystallization*, 3rd ed., Butterworth-Heinemann, Oxford, UK, 1997.
- [30] M. Alifanti, J. Kirchnerova, B. Delmon, *Appl. Catal. A* 245 (2003) 231.
- [31] H. Arai, T. Yamada, K. Eguchi, T. Seiyama, *Appl. Catal. A* 26 (1986) 265.
- [32] L. Marchetti, L. Forni, *Appl. Catal. B* 15 (1998) 179.
- [33] M. Alifanti, J. Kirchnerova, B. Delmon, D. Klvana, *Appl. Catal. A* 262 (2004) 167.
- [34] S.H. Liang, F. Teng, G. Bulgan, R.L. Zong, Y.F. Zhu, *J. Phys. Chem. C* 112 (2008) 5307.